Journal of
Materials Chemistry C

PAPER

View Article Online
View Journal | View Issue

Cite this: *J. Mater. Chem. C*, 2026, **14**, 5537

Long photocarrier lifetimes in $CsPbBr_3$ films deposited by a machine-learning-assisted IR-laser molecular beam epitaxy process

Shizuka Suzuki,[a] Toshihiro Sato,[b] Hideomi Koinuma,[c] Ryuzi Katoh[d] and Ryota Takahashi *[a]

Received 2nd September 2025,
Accepted 23rd January 2026

DOI: 10.1039/d5tc03279b

rsc.li/materials-c

We investigated a machine-learning-assisted IR-laser molecular beam epitaxy (IR-MBE) process to extend the photocarrier lifetime of halide perovskite $CsPbBr_3$ films. In this method, the raw material powder placed in a vacuum is heated by pulsed IR laser irradiation, thereby depositing thin-film crystals on the heated substrate. A machine-learning approach was employed to explore the growth window that enhances the crystallinity of IR-MBE-grown $CsPbBr_3$ films and maximizes their functional properties. A closed-loop operation based on Bayesian optimization was performed to explore the growth window by autonomously tuning three synthesis parameters: substrate temperature, nitrogen pressure, and deposition rate. Twenty trial depositions led to the detection of a growth window that drastically improved the crystallinity of the $CsPbBr_3$ film. When the $CsPbBr_3$ film was deposited under optimum conditions, the optical absorption rate of the excitons increased, and the photoluminescence emission efficiency improved. Furthermore, time-resolved microwave photoconductivity measurements revealed a long photocarrier lifetime of 40.4 μs, which was comparable to that of bulk $CsPbBr_3$ single crystals, even though the $CsPbBr_3$ film was polycrystalline, revealing that the generation of defects to promote nonradiative recombination was suppressed. The IR-MBE method assisted by Bayesian optimization is a powerful synthetic process that improves the quality of halide perovskite films and maximizes the functional properties of the material itself.

Introduction

Halide perovskites have attracted considerable attention as semiconductor materials since their discovery in 2009.[1] According to early solar cell reports, the electrochemical cell structure was similar to that of dye-sensitized solar cells, which consisted of a liquid containing iodide ions. Subsequently, the device structure became solid, and the photoelectric conversion efficiency exceeded 10%.[2] Furthermore, the development of binary and ternary chemical compositions of perovskite materials[3–5] and the passivation effect at the electron transport layer (ETL) and hole transport layer interfaces[6,7] have led to photoelectric conversion efficiencies exceeding 20%. In particular, the introduction of the two-step method[8,9] and the antisolvent method[10,11] has significantly improved the crystallinity of perovskite films, achieving a high photoelectric conversion efficiency exceeding 25%.[12,13] Materials with excellent photoelectric conversion efficiency have been applied not only to solar cells but also to devices such as light-emitting diodes (LEDs)[14,15] and lasers.[16]

Photocarrier lifetime is an important physical parameter for investigating the quality of the semiconductor crystal of a photoelectric conversion material. This is because the parameter is determined by the balance between radiative and non-radiative recombination, which is caused by the formation of defect structures. When the crystallinity of a semiconductor is poor, deep defect levels are generated in the bandgap. Photoexcited electrons are trapped at the defect levels, inducing non-radiative recombination; consequently, the photocarrier lifetime decreases.[17] To improve the performance of photoelectric conversion devices such as photocatalysts, solar cells, and LEDs, the development of thin-film processes is actively promoted to extend the photocarrier lifetime. For example, during the development of a water-splitting photoelectrode using a photocatalytic $SrTiO_3$ film, the formation of crystal defects in the $SrTiO_3$ film is suppressed by optimizing the deposition temperature and pressure during film growth, leading to a longer photocarrier lifetime and improved

---

[a] College of Engineering, Department of Electrical and Electronic Engineering, Nihon University, Fukushima, 963-8642, Japan
E-mail: takahashi.ryota@nihon-u.ac.jp
[b] Vacuum Products, Tokyo, 187-0012, Japan
[c] Smart Combinatorial Technology, Tokyo, 105-0014, Japan
[d] College of Engineering, Department of Chemical Biology and Applied Chemistry, Nihon University, Fukushima, 963-8642, Japan

photoconductivity.[18] Ultimately, this improvement enhances the internal quantum efficiency of the water-split photoelectrode.[19,20] Therefore, it is particularly important to develop a film fabrication process that efficiently optimizes process parameters, such as substrate temperature and pressure, even for halide perovskite films, and extends photocarrier lifetimes.

In this study, we attempted to extend the photocarrier lifetime of halide perovskite $CsPbBr_3$ films using two methods. The first approach employs a unique film synthesis using the pulsed IR laser molecular beam epitaxy (IR-MBE) method. The raw powder is placed in a vacuum and heated by pulsed IR laser irradiation, resulting in the evaporation of the heated substrate. This process has been developed to gently deposit functional films of organic materials and ionic liquids.[21–23] Furthermore, this process can be employed to deposit halide perovskite materials such as $MAPbI_3$,[24,25] $CsPbBr_3$,[26,27] and $CsPbI_3$[27] films. In particular, the $CsPbBr_3$ films deposited by IR-MBE exhibited a significantly longer photocarrier lifetime of 35 μs according to the time-resolved microwave conductivity (TRMC) measurements, revealing the high crystallinity of the $CsPbBr_3$ films.[26] However, this process requires complex layering, in which a 50-nm CsBr thin film is deposited prior to the $CsPbBr_3$ film deposition, otherwise, the impurity phase $CsPb_2Br_5$ crystallizes in the $CsPbBr_3$ film, deteriorating its optical properties. Therefore, it is essential to develop a simple film deposition process within the growth window in which stoichiometric $CsPbBr_3$ films can grow in a self-organized manner while suppressing defect formation. The growth window indicates the range of optimal process conditions, such as temperature, pressure, and the flux amount, that allow the stable growth of high-quality thin films in vacuum deposition. For example, when complex oxides such as $SrTiO_3$ and $BaTiO_3$ are deposited using a growth window, the chemical composition approaches the stoichiometric composition, improving the crystallinity and surface flatness of the film crystal and leading to a significant improvement in the functional properties of the film device.[28–30] If a $CsPbBr_3$ film is deposited within the growth window, it is possible to synthesize a $CsPbBr_3$ film with good crystallinity, a uniform chemical composition, and fewer defects, directly leading to an improvement in film functionality.

To explore the growth window efficiently, a second approach was adopted using Bayesian optimization. Bayesian optimization is a method that can start an estimation from relatively small experimental data among various machine learning methods. Recently, this method has been widely used in materials research to optimize material synthesis processes for superconducting materials,[31] electrode materials,[32,33] phase-change materials,[34] two-dimensional materials,[35–37] and phosphors.[38] In Bayesian optimization, a function that returns a predicted value for the input data is created using a Gaussian process regression. It is possible to express complex responses that cannot be obtained using linear regression. In Gaussian process regression, the predicted value μ and standard deviation σ of the data are calculated from experimental data. Subsequently, the next measurement plan was proposed based on an acquisition function that considers them. The optimization of process parameters that maximize the functions and physical properties of materials can be accelerated by combining Bayesian optimization with the expected improvement (EI) acquisition function applied to the IR-MBE method.

In this study, we performed a closed-loop operation using experimental crystallinity data obtained from X-ray diffraction (XRD) to search for a growth window that improves the crystallinity of $CsPbBr_3$ films grown by IR-MBE. Two growth parameters, the substrate temperature and nitrogen pressure, were chosen to form a growth window.[28–30] The deposition speed was chosen to suppress the evaporation of volatile CsBr composition.[39] Bayesian optimization was performed to determine the three synthesis parameters that maximized the $CsPbBr_3$ (110) reflection intensity as measured by XRD. The closed-loop operation was repeated 20 times, resulting in the detection of the growth window. The $CsPbBr_3$ film deposited in the optimized growth window exhibited improved film crystallinity and reduced defect density. As a result, non-radiative recombination was suppressed, and the photoluminescence (PL) emission efficiency increased. TRMC measurements revealed a long photocarrier lifetime of 40.4 μs for the $CsPbBr_3$ film.

Experimental

The $CsPbBr_3$ film was prepared by IR-MBE (Vacuum Products: Double laser PVD)[40] on $SrTiO_3$(001) substrates that were wet-etched in buffered NH_4F-HF to obtain a well-defined surface termination (Shinkosya, ST-AS-15S).[41,42] During the deposition, the substrate was heated using an infrared semiconductor laser at a wavelength of 1060 nm (SPI lasers, G4, 200W).[30,43] The laser power was controlled using a proportional-integral-differential (PID) controller to maintain the desired temperature.

$CsPbBr_3$ powder (Tokyo Chemical Industry Co., C3569) was placed in a quartz crucible as the raw material for film deposition and irradiated with a continuous-wave (CW) IR laser at a wavelength of 1060 nm (SPI lasers, G4, 40W).[26,27] During the deposition, a CW IR laser was electrically chopped at a frequency of 10 Hz with a pulse duration of 50 ms. The deposition rate was monitored using a quartz crystal oscillator (INFICON STM-2). To precisely control the amount of deposition and maintain the deposition rate, the IR laser power was automatically tuned using a PID controller.[26,27]

The film orientation and lattice parameters of the $CsPbBr_3$ film were analyzed using Cu Kα XRD and wide-range reciprocal space mapping. All the XRD measurements were performed using a Rigaku SmartLab XRD instrument at room temperature. The film thicknesses were determined using a stylus profiler (Kosaka Laboratory: ET200A). The optical transmittance of the $CsPbBr_3$ films was analyzed using a UV-visible microspectrometer (JASCO, MSV-5700). The surface morphologies were analyzed using scanning electron microscopy (SEM) energy-dispersive X-ray spectroscopy (EDS) (JEOL, JSM-IT200). The Cs/Pb ratio was calibrated by using commercial $CsPbBr_3$ powder (Tokyo Chemical Industry Co., C3569).

PL measurements were performed using a custom-built fluorescence spectrometer.[44] For excitation, an LED lamp at 365 nm (Hamamatsu: LC-L1) was focused on the film samples at 25.1 mW cm^{-2}. The luminescence from the sample was transferred to a monochromator (Acton: Spectra Pro 150) using a quartz glass fiber. UV-cut filters (L40 and L42) were used between the sample and the detector to eliminate excitation light. The excitation and luminescence intensities were tuned using neutral-density (ND) filters. All PL measurements were performed in the same configuration using a relatively long focus lens. The difference in emission intensity corresponds to that PL emission yield, *i.e.*, lower emission intensity corresponds to a larger contribution from the non-radiative process.

Time-resolved PL (TRPL) was measured by time-correlated single-photon counting (TCSPC). A pulsed 375-nm laser diode (Edinburgh Instruments, EPL-375) was used as the excitation source. The emissions were collected using a cooled high-speed photomultiplier tube detector head for photon counting (Becker & Hickl GmbH: PMC-150-04).

For TRMC measurements, microwaves generated using an oscillator based on a 200-mW Gunn diode (Nakadai MGS-15B) were used as the probe.[26,45–47] The frequency was tuned from 8 to 9 GHz using a varactor diode. The microwaves were directed toward the sample cavity through a waveguide. The third harmonic (355 nm) of a Nd:YAG laser (VM-TIM, VM-200-10-ST) was used for the UV excitation measurements. The laser pulse duration was 10 ns. The pulse intensity was tuned using ND filters ranging from 7.6 × 10^{-3} to 3.9 μJ cm^{-2}. Reflected microwaves were detected using a diode (NEC, IN23WE). The measured signals were processed using a digital oscilloscope (Tektronix: TDS680C) and analyzed on a computer.

Results and discussion

Bayesian optimization of process parameters

Fig. 1(a) illustrates the closed-loop optimization for IR-MBE growth. The $CsPbBr_3$ films are deposited using IR-MBE.[26,27] The three important parameters selected for IR-MBE are substrate temperature, nitrogen pressure, and growth rate. The first two parameters are the most important parameters for forming the growth window for MBE synthesis.[28–30] The remaining growth rate is essential when depositing complex compounds containing volatile elements like CsBr. Depositing films at a faster growth rate suppresses the loss of volatile elements, making it possible to fabricate thin films with a closer stoichiometric composition.[39]

First, the substrate temperature is maintained constant during the deposition process by PID control of the intensity of the IR laser used for heating.[30,43] In the optimization process, the temperature is varied in the range of 150 °C to 300 °C. Second, the pressure is maintained constant during film deposition by the PID control of the amount of nitrogen flowing into the chamber.[40] The nitrogen pressure is optimized

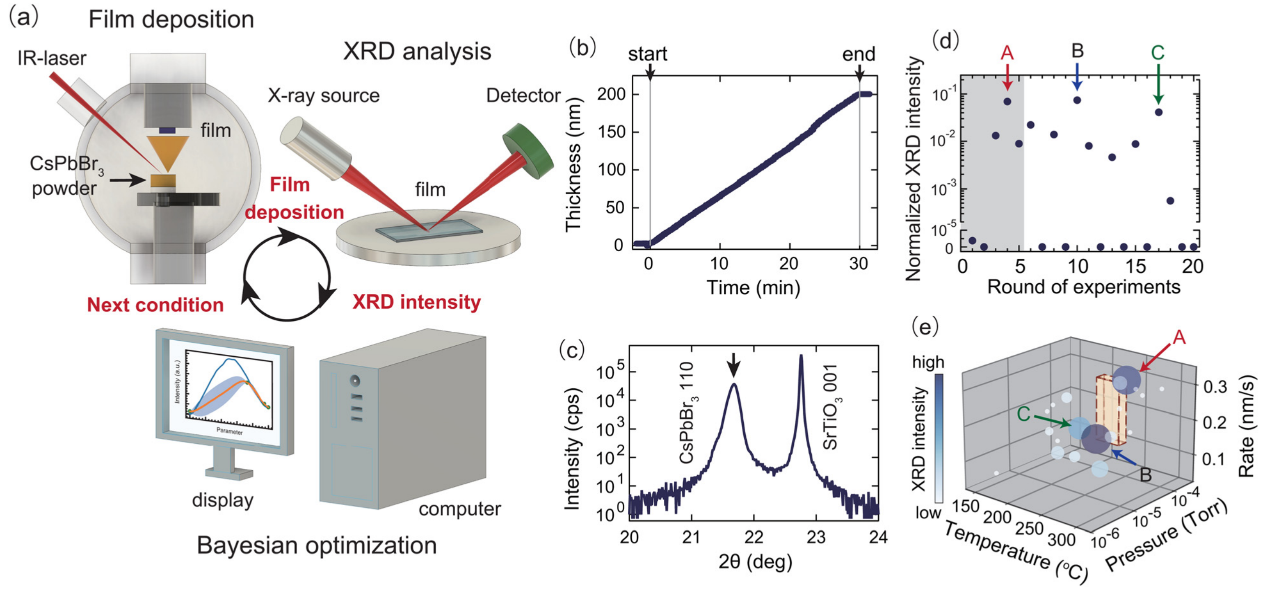

Fig. 1 (a) Schematic of the closed-loop optimization of $CsPbBr_3$ film growth using a machine-learning-assisted IR-MBE technique. A $CsPbBr_3$ film was grown *via* the IR-MBE method. The prepared $CsPbBr_3$ film was characterized by XRD to estimate the crystallinity of the $CsPbBr_3$ film. A Bayesian approach was employed for the prediction of the growth parameters: film growth rate, substrate temperature, and nitrogen pressure. (b) $CsPbBr_3$ film thickness monitored using a quartz crystal oscillator during the $CsPbBr_3$ film growth by IR-MBE. The deposition rate is controllable during the entire deposition. (c) Typical XRD pattern of a poly-crystalline $CsPbBr_3$ film grown on the $SrTiO_3$ (001) substrate. (d) Bayesian optimization of the growth parameter to maximize the normalized XRD intensity. The gray boxed area denotes the initial five points. (e) Normalized XRD intensity as a function of growth parameters: film growth rate, substrate temperature, and nitrogen pressure. The red dotted line denotes the growth window to form the highly crystalline $CsPbBr_3$ films on the $SrTiO_3$ (001) substrate. The three deposition conditions to synthesize the $CsPbBr_3$ film with good crystallinity are named A, B, and C, as shown in (d) and (e).

in the range of 3.0×10^{-6} to 1.0×10^{-4} Torr. Third, the deposition rate is monitored using an *in situ* thickness monitoring system during the entire deposition process, as shown in Fig. 1(b).[26] From the start of deposition, the irradiation intensity of the pulsed IR-laser for heating is PID-controlled to keep the deposition rate constant at the rate set using the software. The deposition rate is varied within the range of 0.05–0.30 nm s^{-1}. The total thickness of the $CsPbBr_3$ film is fixed at 200 nm using an *in situ* thickness monitoring system.

After the deposition of the $CsPbBr_3$ film by IR-MBE, its crystallinity was quantitatively evaluated by XRD analysis. Fig. 1(c) shows a typical XRD pattern of $SrTiO_3$ (001). The $CsPbBr_3$ (110) peak is clearly observed on the low-angle side of the $SrTiO_3$ (001) peak. The previous study using an α-Al_2O_3 substrate suggests that the $CsPbBr_3$ (110) peak is strongest in the XRD pattern and sensitive to the film crystallinity.[26] The reflection has been selected to evaluate the crystallinity of the $CsPbBr_3$ film. We note that the full width at half maximum (FWHM) is the most standard parameter to quantitatively compare the film crystallinity. However, during the process optimization, XRD peaks are sometimes not observed, making it impossible to input the FWHM value into Bayesian optimization calculation. Therefore, in this study, the XRD peak intensity was adopted as the input value.

The film peak intensities should vary from sample to sample, depending on the quality of the $SrTiO_3$ substrate and the alignment of the XRD patterns. Therefore, the peak intensities of the films were normalized to the intensity of the $SrTiO_3$ (001) reflection. The normalized intensity was used as the criterion for evaluating the crystallinity of $CsPbBr_3$ films.

Three synthesis parameters (substrate temperature, nitrogen pressure, and deposition rate) were optimized using Bayesian optimization to maximize normalized peak intensity. The EI function was used as the acquisition function for the Bayesian optimization.[38] Five synthesis conditions were randomly selected as the initial values. Using the measurement results of the initial five points, the mean (μ) and variance (σ) of the data were calculated using Bayesian optimization based on Gaussian process regression. The acquisition function was calculated from these values, and the three synthesis parameters that maximized the value of the acquisition function obtained from the sixth trial were predicted. The closed-loop operation of thin-film synthesis by IR-MBE, structural evaluation by XRD, and data prediction by Bayesian optimization were repeated 20 times to search for the growth window of the $CsPbBr_3$ film.

Fig. 1(d) shows the XRD intensity for each trial. The gray hatched area denotes the results of the first five trials. To determine how many samples are needed to reach the growth window, the XRD intensity was plotted as a function of the total number of samples.[31] After obtaining the initial five points, a closed-loop operation using Bayesian optimization was repeated. The synthesis parameters for enhancing the XRD intensity of the $CsPbBr_3$ films were determined in the 4th, 10th, and 17th trials. Fig. 1(e) shows the XRD intensity for each synthesis parameter used in the 20 experiments. A tendency for the XRD intensity to increase is observed in the nitrogen pressure region around 10^{-4} Torr and the substrate temperature region at approximately 200 °C. The region indicated by the red dotted line in Fig. 1(e) is expected to be the growth window where the crystallinity of the $CsPbBr_3$ film increases.

Structural analysis of $CsPbBr_3$ films

The three recommended synthesis conditions suggested by Bayesian optimization are denoted as A, B, and C, as shown in Fig. 1(d and e). The crystal structures of the $CsPbBr_3$ films deposited under conditions A, B, and C were evaluated by XRD. Fig. 2(a–c) show the XRD patterns of $CsPbBr_3$ films deposited under conditions A, B, and C. Polycrystalline $CsPbBr_3$ films with cubic structures were grown on the $SrTiO_3$ (001) substrate. No peaks derived from the impurity phase are observed for the $CsPbBr_3$ films deposited under conditions A and B, whereas the $CsPbBr_3$ film deposited under condition C precipitates a *c*-axis-oriented $CsPb_2Br_5$ impurity phase. Furthermore, the absence of impurity phase precipitation suggests that the Cs/Pb ratio of the $CsPbBr_3$ films deposited under conditions A and B should be close to 1. SEM-EDS analysis shown in Fig. S1 has revealed that the Cs/Pb ratios under conditions A, B, and C were measured to be 0.997, 0.995, and 0.921, respectively, supporting the presence or absence of impurity $CsPb_2Br_5$ phase precipitation observed by XRD analysis. Therefore, the red boxed regions in Fig. 1(e) formed under conditions A and B, as identified by Bayesian optimization, represent the growth window, indicating that the chemical composition of the $CsPbBr_3$ films approaches the stoichiometric composition in the red boxed region. Moreover, under the growth window using condition A, the high crystallinity film was reproduced, as shown in Fig. S2, presenting no impurity peak and the same intensity as the $CsPbBr_3$ (110) orientation.

When comparing the XRD peak intensity distributions of the three samples in Fig. 2(a–c), the $CsPbBr_3$ film deposited under condition B has relatively high peak intensities for the (110) and (111) orientations, whereas the $CsPbBr_3$ film deposited under condition A has a higher peak intensity for the (001) orientation. In the chemical vapor deposition (CVD) and pulsed laser deposition (PLD) methods, $CsPbBr_3$ films deposited on $SrTiO_3$(001) substrates can grow epitaxially along the *c*-axis.[48–50] The $CsPbBr_3$ film deposited under condition A is expected to grow in an in-plane orientation.

Fig. 2(d) shows the wide-range reciprocal space mapping of the $CsPbBr_3$ film deposited under condition A along the HOL plane of the $SrTiO_3$ lattice. Generally, in reciprocal space mapping, ring-shaped peaks are observed in polycrystalline thin films with no in-plane orientation, whereas spot-shaped diffraction points are observed in single-crystalline films with a uniform in-plane orientation. In Fig. 2(d), weak ring-shaped peaks are observed around the (110), (002), and (112) reflections, suggesting the presence of domains randomly aligned along the in-plane direction. In contrast, strong spot-shaped peaks are also observed, revealing the presence of domains with an in-plane orientation.

Fig. 2(e) shows the relationship between the in-plane orientation of the *c*-axis-oriented $CsPbBr_3$ film and the $SrTiO_3$(001) substrate.

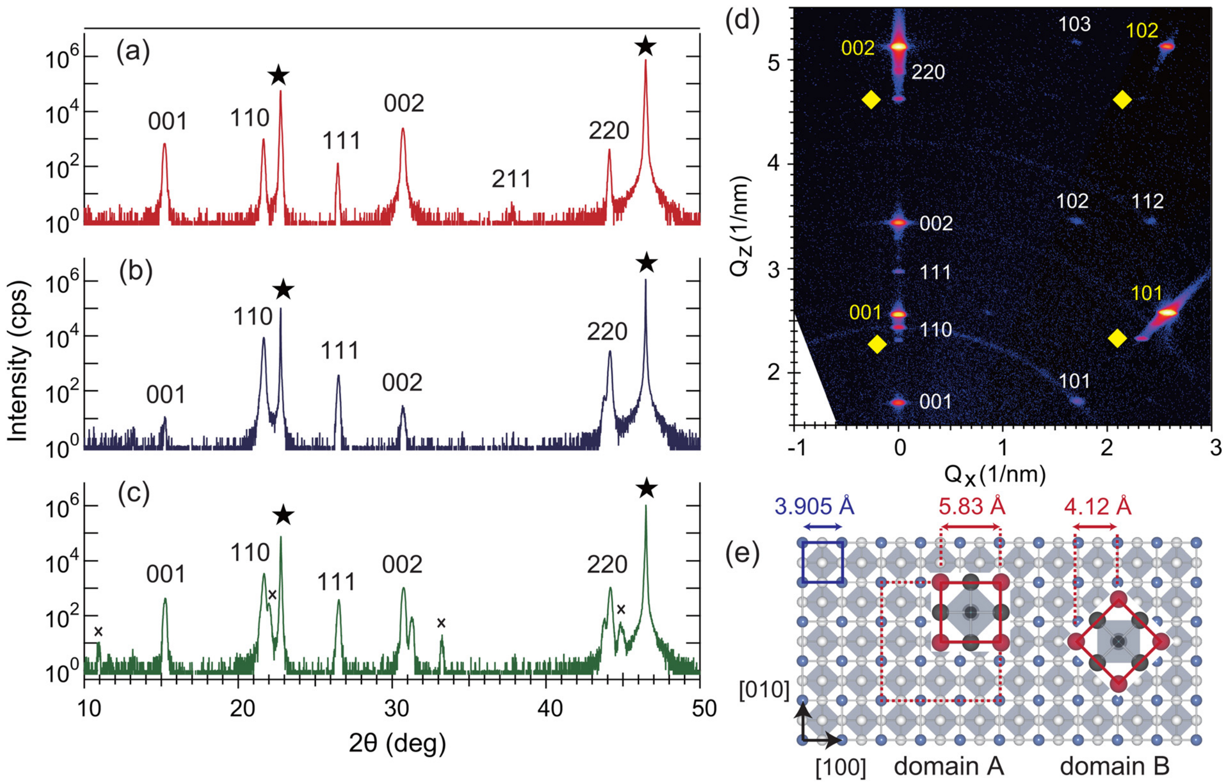

Fig. 2 (a), (b) and (c) XRD patterns of $CsPbBr_3$ films grown under conditions A, B and C, respectively. "★" and "×" denote the reflection of the $SrTiO_3$ substrate and the $CsPb_2Br_5$ impurity phase, respectively. (d) Wide-range reciprocal space mapping of a $CsPbBr_3$ film grown under condition A on the $SrTiO_3$ substrate. White and yellow are the reflection of the film and the substrate, respectively. "◆" denotes the K_β reflection of the substrate crystal. (e) Schematic of the in-plane relationship between the $SrTiO_3$(001) substrate (blue) and the $CsPbBr_3$ (001) film (red).

The lattice constant of the cubic $CsPbBr_3$ is 5.83 Å, whereas that of the cubic $SrTiO_3$ substrate is 3.905 Å.[48–50] As in previous reports on $CsPbBr_3$ films prepared by PLD and CVD, the two unit cells of $CsPbBr_3$ match incommensurately with the three unit cells of $SrTiO_3$.[48–50] The lattice mismatch coefficient is calculated to be −0.5%. Here, the in-plane orientation is called domain A. In contrast, when $CsPbBr_3$ is rotated by 45° with respect to the $SrTiO_3$ substrate, the lattice mismatch is estimated to be +5.6%. Here, the in-plane orientation is called domain B. Therefore, in a $CsPbBr_3$ film on a $SrTiO_3$ (001) substrate, the two in-plane orientations of domains A and B might coexist.

In the wide-range reciprocal space mapping shown in Fig. 2(d), in addition to the peaks of the $SrTiO_3$ substrate, the (101), (102), and (103) reflection peaks of the $CsPbBr_3$ films are clearly observed on the asymmetric plane, indicating the presence of domain A, as illustrated in Fig. 2(e). Furthermore, the (112) peak of $CsPbBr_3$ is observed, revealing the presence of domain B. Fig. S3 shows the wide-range reciprocal space mapping measured along the HHL plane of the $SrTiO_3$ lattice. Fig. 2(e) shows the coexistence of the two domain structures.

Fig. S4(a) and (b) show wide-range reciprocal space mappings of the $CsPbBr_3$ films deposited under conditions B and C. In addition to the two domain structures shown in Fig. 2(d), diffraction peaks originating from the [110] and [111] orientations are observed together with the [001]-oriented domain. This indicates that the proportion of the [110] and [111] orientations is higher than that of the $CsPbBr_3$ film deposited under condition A. Therefore, the difference in the (001) peak intensity observed in the XRD patterns in Fig. 2(a–c) reflects the degree of *c*-axis orientation with an in-plane orientation. The $CsPbBr_3$ film prepared under condition A does not contain any impurity layers and exhibits the strongest *c*-axis orientation. The structural XRD analysis suggests that the functional properties of the $CsPbBr_3$ film prepared under condition A are superior to those of the other two samples.

Optical absorption and luminescence analysis of $CsPbBr_3$ films

Fig. 3(a) shows Tauc plots of the $CsPbBr_3$ films deposited under conditions A, B, and C. The bandgap of each film is estimated to be 2.3 eV, which is consistent with the reported bandgaps of the $CsPbBr_3$ films.[48–50] The exciton absorption peak is observed at a higher energy than that of the bandgap edge. The exciton absorption rate is the highest in the $CsPbBr_3$ film deposited under condition A. In contrast, the exciton absorption rate is attenuated in the films deposited under conditions B and C. Excitons are generally scattered by defects and the precipitation of impurity phases,[51] suggesting that the $CsPbBr_3$ film deposited under condition A has high film quality. The optical absorption data are consistent with the results of the structural evaluation by XRD.

Fig. 3(b) shows the PL spectra measured using a 365 nm excitation light for the $CsPbBr_3$ films deposited under

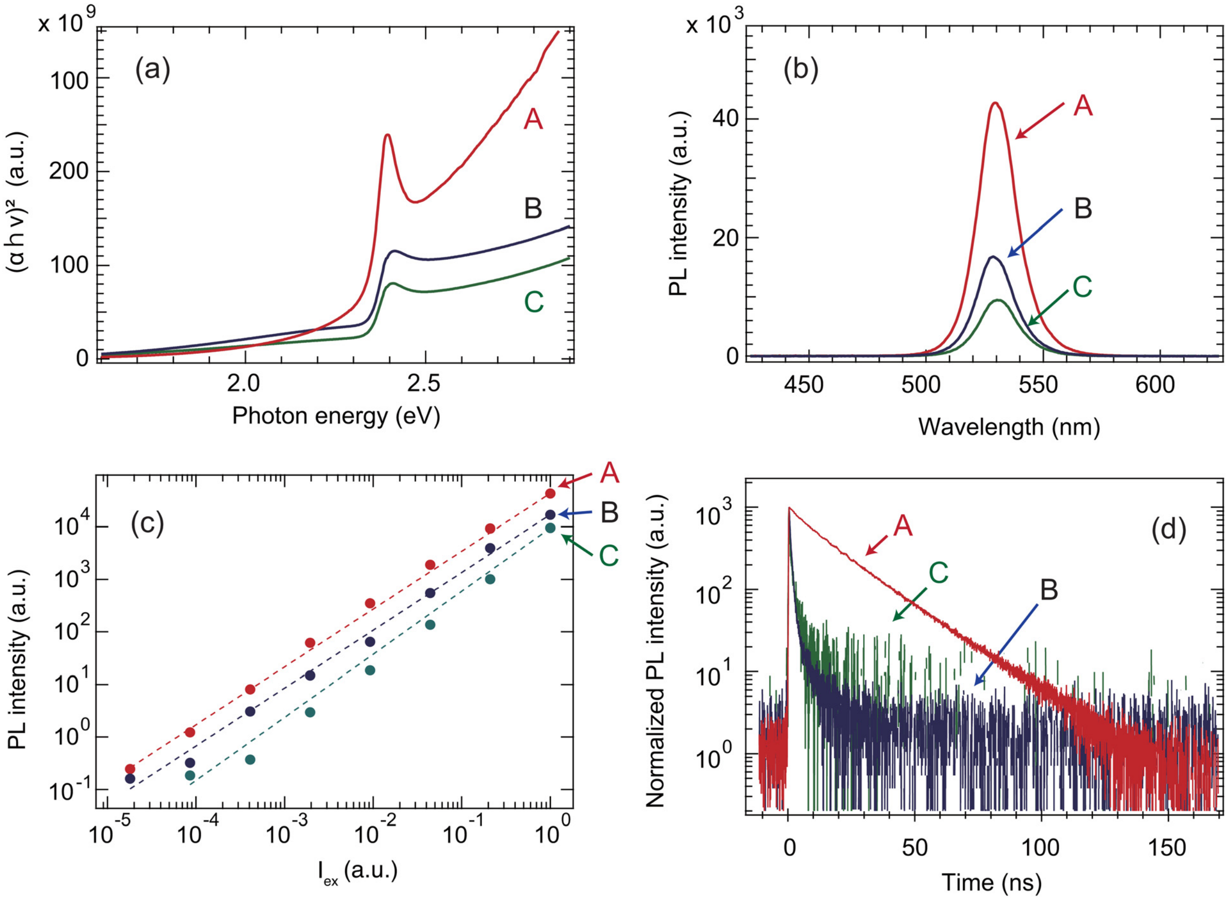

Fig. 3 Tauc plots (a), PL emission spectra (b), excitation laser energy dependences on PL emission intensity at 530 nm (c), and TRPL profiles (d) of the $CsPbBr_3$ films grown under conditions A, B, and C. The dotted lines in (c) denote the fitting curve using the power law.

conditions A, B, and C. Strong PL emission is observed at 530 nm for all $CsPbBr_3$ films, and no shift is observed in the emission wavelength. Comparing the emission intensities, the PL intensity of the $CsPbBr_3$ film deposited under condition A is 40,515 counts, the strongest intensity, whereas the intensities of the films deposited under conditions B and C are smaller at 16 967 and 9 476 counts, respectively. The same optical configuration was used for the three measurements. Therefore, the difference in luminescence intensity corresponds to the difference in luminescence yield. If the relative quantum efficiency of the $CsPbBr_3$ film deposited under condition A is considered as 100%, the $CsPbBr_3$ films deposited under conditions B and C have lower luminescence efficiencies of 41.9% and 23.4%, respectively.

Fig. 3(c) shows the excitation light intensity dependence of the PL emission intensity at 530 nm for the $CsPbBr_3$ films prepared under conditions A, B, and C when the wavelength of the excitation light is 365 nm. The excitation light intensity dependence is useful for identifying the recombination pathway of photoexcited carriers in the crystal because the PL emission intensity is experimentally proportional to the power law ($I_{PL} \propto I_{exc}{}^{\alpha}$).[52] Therefore, the power factor α is a parameter that reflects the carrier recombination process. The PL emission intensities of all $CsPbBr_3$ films change linearly in proportion to the excitation light intensity, and no shift is observed in the emission peak. The α values of the $CsPbBr_3$ films deposited under conditions A, B, and C are estimated to be 1.1, 1.1, and 1.2, respectively. No significant nonlinear behavior due to recombination influenced by free carriers at the impurity level is observed, as shown in Fig. 3(c).

Fig. 3(d) shows the TRPL profiles measured using TCSPC for the $CsPbBr_3$ films deposited under conditions A, B, and C. The transient PL profile was fitted using an exponential function with the following time constant:[44,53]

$$I_{PL} = A\exp\left\{-\left(\frac{t}{\tau}\right)^{\alpha}\right\} \quad (1)$$

where t is the time, A is the emission intensity, and α is the distribution parameter. The ideal TRPL profile has an α value of 1, and the PL intensity decays with a single exponential function. When α deviates from 1, it implies that non-radiative recombination occurs because of the formation of defect levels. The fitting results are shown in Fig. S5. The α values of the $CsPbBr_3$ films deposited under conditions A, B, and C are estimated to be 0.88, 0.70, and 0.34, respectively. The profile of the $CsPbBr_3$ film deposited under condition A is the closest to a single exponential, and a linear behavior is observed in the PL intensity in the logarithmic graph. In contrast, the other two

TRPL profiles deviate from a single exponential, suggesting the formation of multiple excitation levels due to the formation of defect structures, and the PL emission is strongly affected by the excitons in the $CsPbBr_3$ films.

From the TRPL profiles of the $CsPbBr_3$ films deposited under conditions A, B, and C, the half-lives at which the PL intensity reaches half of the maximum intensity are estimated to be 10.6, 0.6, and 0.3 ns, respectively. The calculated results correlate with the trend in the relative luminescence efficiency of the PL spectra shown in Fig. 3(b). The $CsPbBr_3$ film deposited under condition A exhibits the longest luminescence lifetime. In contrast, the $CsPbBr_3$ film deposited under condition C has more defects that cause non-radiative recombination owing to the precipitation of impurity phases of $CsPb_2Br_5$ with a CsBr deficiency. Consequently, the PL lifetime is the shortest. The crystallinity obtained from the XRD analysis shown in Fig. 2 correlates with the occurrence of nonradiative recombination, strongly affecting not only the shape of the TRPL profile but also the emission lifetime.

TRMC analysis of $CsPbBr_3$ films

The photoconductivity of the $CsPbBr_3$ films was evaluated using TRMC measurements. TRMC is a time-resolved microwave conductivity that measures the electrical conductivity (σ) of charge carriers generated in a film sample by irradiation with a UV pulse laser from the amount of microwave absorption. TRMC measurement is an effective method for quantitatively evaluating charge carrier dynamics in various halide perovskite thin films and single crystals.[26,47,54–60]

When a sample is irradiated with a UV laser, microwaves are absorbed owing to carrier generation. The amount of absorption ($-\Delta P/P$) is expressed using the following equation:

$$-\frac{\Delta P}{P} = -K\sigma = K' N_e \sum \mu \tag{2}$$

where K and K' are constants, N_e is the number of charges, and μ represents the sum of the carrier mobilities of positive and negative charges. Therefore, the TRMC transient profile contains signals related not only to the amount and mobility of charge carriers in the film but also to the kinetics of the electron–hole recombination and charge carrier trapping processes. Immediately after photoexcitation by irradiation with the excitation UV pulse laser, N_e reaches a maximum value and represents the generation rate of mobile charges (Φ_{CG}). When the excitation light is completely absorbed by the sample, eqn (2) can be expressed as follows:

$$-\frac{\left(\frac{\Delta P}{P}\right)_{\max}}{I_{ex}} = K'' \Phi_{CG} \sum \mu \tag{3}$$

where K'' is a constant and I_{ex} is the UV laser intensity. Using this equation, the effective mobility of halide perovskite films, which strongly depends on crystallinity and impurities, can be estimated without depositing an electrode film on the film surface. Another advantage of TRMC for evaluating halide perovskite films is the investigation of dynamics related to the recombination and trapping of photoinduced charge carriers. The decay of the TRMC represents the photocarrier lifetime, which varies depending on the balance between radiative and non-radiative recombination induced by the generation of defect levels. As a result, non-radiative recombination is suppressed by reducing the defect density, and the photocarrier lifetime is extended. Therefore, the photocarrier lifetime value of halide perovskite films is an important parameter that allows for the comparison of the crystallinity and mobility of thin films fabricated by different fabrication processes.

Fig. 4(a) shows the transient $-\Delta P/P$ profiles of $CsPbBr_3$ films deposited under conditions A, B, and C. To suppress secondary hole and electron recombination, all profiles were measured at a low excitation light intensity of 0.03 $\mu J\ cm^{-2}$. When the $CsPbBr_3$ film is irradiated under 355-nm excitation light, mobile carriers are generated, which absorb the microwaves. The $-\Delta P/P$ value rises instantaneously at 0 μs when the excitation laser is irradiated and reaches a maximum value $(-\Delta P/P)_{max}$. Subsequently, the $-\Delta P/P$ value gradually decreases because of hole and electron recombination and trapping. Here, the half-life of $-\Delta P/P$ is defined as the photocarrier lifetime. The half-lives of the $CsPbBr_3$ films deposited under conditions A and B are significantly long, at 40.4 and 20.3 μs, respectively, whereas the half-life of the $CsPbBr_3$ film deposited under condition C is 0.2 μs, which is about two orders of magnitude shorter than that of the other two samples.

Furthermore, the $(-\Delta P/P)_{max}$ of the $CsPbBr_3$ film deposited under condition A is 8.2×10^{-5}, whereas the $(-\Delta P/P)_{max}$ values of the $CsPbBr_3$ films deposited under conditions B and C are 3.3×10^{-5} and 2.4×10^{-5}, respectively. As suggested by the structural analysis data shown in Fig. 2 and the optical analysis data shown in Fig. 3, the $CsPbBr_3$ film prepared under condition A, which has the best film quality, exhibits the highest photoconductivity. In contrast, the $CsPbBr_3$ film deposited under condition C exhibits the precipitation of the $CsPb_2Br_5$ impurity phase, deteriorating its photoconductivity characteristics.

Fig. 4(b) shows the excitation intensity dependence of the normalized $((-\Delta P/P)_{max}/I_{ex})$ for the $CsPbBr_3$ film prepared under condition A, which exhibits the maximum value of $(-\Delta P/P)_{max}$. When the excitation light energy is high, the value of $((-\Delta P/P)_{max}/I_{ex})$ is small because of secondary hole–electron recombination. As the excitation light intensity decreases, the effect of secondary hole–electron recombination weakens, and $((-\Delta P/P)_{max}/I_{ex})$ becomes larger and saturates at a maximum value. A bell-shaped excitation light intensity dependence is observed for $CsPbBr_3$ films deposited by PLD.[47] In PLD, the kinetic energy of the plume is high and the plume responds to the $CsPbBr_3$ film, forming defects in the thin film.[61,62] In contrast, in IR-MBE, the $CsPbBr_3$ raw material is heated using a pulsed IR laser, and thin-film crystals can be deposited under much milder conditions than that in PLD; thus, the formation of defects is suppressed. The dependence of the bell shape on the excitation light intensity is not shown in Fig. 4(b).

A significant benefit of TRMC measurements is that the effective mobility and half-life of $\Phi_{CG} \sum \mu$ can be quantitatively compared with previously reported values using eqn (2),

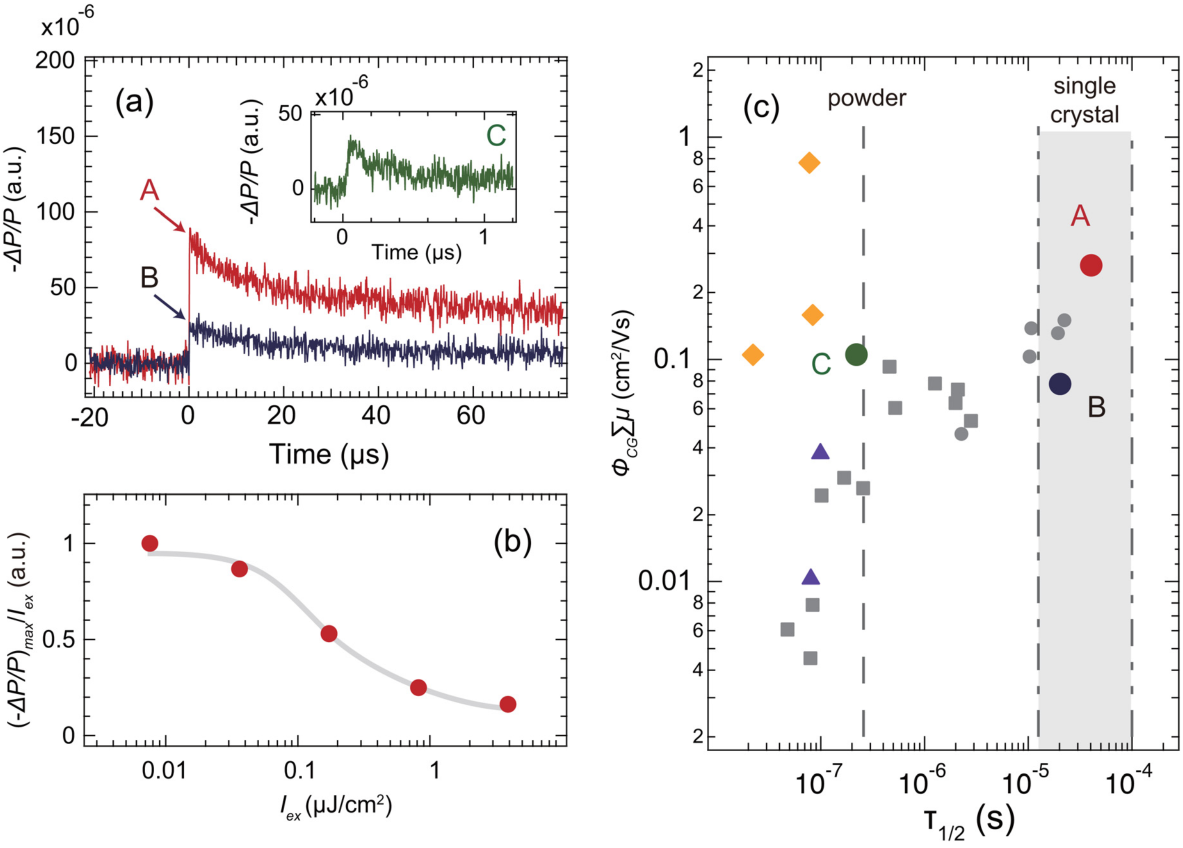

Fig. 4 (a) Transient profiles of signals for $CsPbBr_3$ films grown under conditions A and B. The inset shows the transient $-\Delta P/P$ signal under condition C. (b) Normalized $((-\Delta P/P)_{max}/I_{ex})$ value as a function of the excitation laser intensity (I_{ex}) of the $CsPbBr_3$ film grown under the optimum condition of A. (c) $\Phi_{CG}\sum\mu$ of the $CsPbBr_3$ films as a function of $\tau_{1/2}$. The circle and square denote the excitation laser energies of 0.03 and 0.68 μJ cm^{-2}, respectively. For comparison, the yellow diamonds and purple triangles plot the TRMC results for the $CsPbBr_3$ films in ref. 58 and 59. The gray dashed and dash-dotted lines denote the measurement data of the $CsPbBr_3$ powder and single-crystal samples, respectively. The double-dash-dotted lines denote the reported $\tau_{1/2}$ of the $CsPbBr_3$ single-crystal sample in ref. 64. The gray area represents the photocarrier lifetime of $CsPbBr_3$ single-crystal samples.

making it possible to determine the quality of the film. Using a reference sample of the anatase thin film, $\Phi_{CG}\sum\mu$ was calculated[46,63] and plotted as a function of the half-life of the TRMC signal. As shown in Fig. 4(c), the $\Phi_{CG}\sum\mu$ values of films deposited under conditions A, B, and C were estimated to be 0.27, 0.08, and 0.11 $cm^2\ V^{-1}\ s^{-1}$, respectively. The values of $\tau_{1/2}$ were 40.4, 20.3, and 0.2 μs. In addition to the three samples, the TRMC measurements of a series of $CsPbBr_3$ films prepared by IR-MBE were plotted for comparison. To perform high-throughput screening of the TRMC signals of several $CsPbBr_3$ films, measurements were performed at two excitation light intensities. The gray circles and squares show the TRMC results measured at 0.03 and 0.69 μJ cm^{-2}, respectively. From the overall plot, as the film quality improves, the defect density decreases and nonradiative recombination is suppressed, leading to longer $\tau_{1/2}$ values and larger $\Phi_{CG}\sum\mu$ values. This means that the high-quality $CsPbBr_3$ film is plotted in the upper-right position in Fig. 4(c) and the low-quality $CsPbBr_3$ film is plotted in the lower left position. The formation of defects reduces the $\Phi_{CG}\sum\mu$ and $\tau_{1/2}$ values due to the nonradiative recombination.

To reconfirm that the $\tau_{1/2}$ value of the measured TRMC signal is a parameter derived from the film quality of $CsPbBr_3$, the $\tau_{1/2}$ values of the commercial $CsPbBr_3$ powder and single crystals are plotted in Fig. 4(c). The gray dashed and dot-dashed lines show the measurement data for the $CsPbBr_3$ powder and single-crystal samples, respectively.[47] The two gray dot dashed lines represent the reported value for the $CsPbBr_3$ single-crystal sample.[64] The $\tau_{1/2}$ values of the commercial powder and single crystal are 0.258 and 13.4 μs, respectively. The improvement in crystallinity suppresses nonradiative recombination and extends the photocarrier lifetime. Comparing the literature data with those of the $CsPbBr_3$ film, the $\tau_{1/2}$ of the $CsPbBr_3$ films deposited under conditions A and B are located in the gray area, which denotes the photocarrier of the $CsPbBr_3$ single crystal. When the mobility is 0.27 $cm^2\ V^{-1}\ s^{-1}$, the measurement temperature is 300 K, and the measurement frequency is 8.5 GHz, the TRMC probing depth is estimated to be 9.1 nm by extrapolating from ref. 54 and 60. Then, the diffusion constant D, which changes depending on the mobility, can be estimated from the following Einstein equation ($D = \mu k_B T/q$), where k_B is the Boltzmann constant, T is the temperature, and q is the elementary charge. When the mobility μ is 0.1 $cm^2\ V^{-1}\ s^{-1}$, the diffusion coefficient D is calculated to be $33 \times 10^{-3}\ cm^2\ s^{-1}$. The diffusion length L can be calculated from $L = (Dt)^{1/2}$, where t is the time.

Since the time domain measured by TRMC is on the order of microseconds, the diffusion length after 1 μs is estimated to be approximately 500 nm. In other words, even if the penetration depth is only 9.1 nm, the TRMC measurement time domain is sufficient to measure the charge that has diffused into the bulk. From the SEM images shown in Fig. S6, the domain size of the $CsPbBr_3$ films deposited under conditions A, B, and C is approximately 1 μm, which is sufficiently larger than the probing depth. Therefore, the film has a crystallinity comparable to that of a single crystal within the probing depth range.

To further clarify the advantages of the unique film synthesis process of IR-MBE, the previously reported TRMC values of the $CsPbBr_3$ films prepared using the spin-coating method are plotted in Fig. 4(c).[58,59] Both the films contained $CsPbBr_3$ nanoparticles embedded in the matrix. Compared with reported values, the maximum half-life of the $CsPbBr_3$ film deposited by pulsed IR-MBE is two orders of magnitude longer. However, no significant change is observed in the value of $\Phi_{CG}\sum\mu$. The largest $\Phi_{CG}\sum\mu$ shown in Fig. 4(c) is due to the interface between the $CsPbBr_3$ nanoparticles and the TCNQ (7,7,8,8-tetracyanoquinodimethane) ETL.[59] The unique interface formation enhances the value of Φ_{CG}, leading to a large value of $\Phi_{CG}\sum\mu$. For the bare $CsPbBr_3$ films deposited by each process without considering the effect of the interface, the $\Phi_{CG}\sum\mu$ value is 0.16 $cm^2\ V^{-1}\ s^{-1}$, which is almost the same as the $\Phi_{CG}\sum\mu$ obtained by IR-MBE, which is 0.27 $cm^2\ V^{-1}\ s^{-1}$. Both films are polycrystalline and strongly affected by grain boundary scattering. In the IR-MBE method, to further improve $\Phi_{CG}\sum\mu$, it is essential to form a thin film in which the crystals grow in a uniform in-plane direction without domain boundaries such as that of single crystals.

Finally, the half-life of the TRMC was compared with that of the TRPL for the best $CsPbBr_3$ film deposited under condition A. The half-life of TRPL is 10.6 ns, whereas the half-life of TRMC is 40.4 μs, which is about three orders of magnitude longer than that of TRPL. A large difference between the two measurements has been reported not only for $CsPbBr_3$ films[26] but also for single crystals of $MAPbI_3$[55] and $CsPbI_3$ films deposited by vacuum evaporation.[56] TRMC measures the photoconductivity, which is proportional to the time-dependent concentration n and mobility μ of free mobile electrons and holes, by the decay of microwaves. In contrast, the TRPL of the $CsPbBr_3$ films reflects the radiative recombination of excitons. Therefore, the decay obtained by TRMC cannot be directly compared with that obtained by TRPL because the two techniques detect different carrier dynamics.[54] Moreover, particularly for the TRPL, PL emission is caused by the recombination of unrelaxed charges before they are fully trapped, according to the previous report.[65] On the other hand, the TRMC signal of $-\Delta P/P$ is proportional to the product of the mobile charge number and the sum of the carrier mobilities, as shown in eqn (2). As the excited electrons relaxes to trap states, the TRMC signal decreases. However, if the trapped charges were still mobile, the TRMC signal would continue. While the further detailed experimental investigation is necessary, the difference is expected to account for the large difference in lifetimes between TRPL and TRMC. At least, the advantage of TRMC is that it is sensitive to non-radiative recombination because the loss of mobile carriers attenuates the observed signal, whether radiative or non-radiative. Furthermore, the behavior of mobile carriers can be observed continuously throughout the sample, making it sensitive to bulk and defects. Therefore, the mapping shown in Fig. 4(c) is useful for comparing the optical functions of perovskite thin films, which are strongly process-dependent.

Conclusions

We performed a closed-loop operation based on Bayesian optimization to explore the growth window that improves the crystallinity of $CsPbBr_3$ films grown by pulsed IR-MBE. After 20 deposition trials, we succeeded in exploring a growth window that not only improved the film crystallinity but also maximized the functional properties of optical absorption and emission. In particular, photoconductivity was significantly improved by depositing $CsPbBr_3$ films in the growth window. The evaluation of the photocarrier lifetime by TRMC revealed a long photocarrier lifetime of 40.4 μs, which is comparable to that of a single crystal. The synthesis of a thin film with high crystallinity suppressed the formation of defect structures, which cause non-radiative recombination. Consequently, the photocarrier lifetime was significantly extended. This unique film process that extends the photocarrier lifetime plays an important role in enhancing the functions of devices such as solar cells, LEDs, and photocatalyst materials. A film process associated with machine learning for determining the growth window efficiently and quickly is expected to improve the functionality of halide perovskite devices.

Author contributions

Shizuka Suzuki: conceptualization, data curation, formal analysis, investigation, methodology, visualization, writing – original draft, and writing – review and editing; Toshihiro Sato: conceptualization, methodology, software, and writing – review and editing; Hideomi Koinuma: conceptualization, funding acquisition, methodology, and writing – review and editing; Ryuzi Katoh: conceptualization, data curation, formal analysis, funding acquisition, investigation, methodology, writing – original draft, and writing – review and editing; and Ryota Takahashi: conceptualization, data curation, formal analysis, funding acquisition, investigation, methodology, visualization, writing – original draft, writing – review and editing project administration, and supervision.

Conflicts of interest

There are no conflicts to declare.

Data availability

The data supporting this article have been included as part of the supplementary information (SI). Supplementary information is available. See DOI: https://doi.org/10.1039/d5tc03279b.

Acknowledgements

This study was supported by the ATLA Innovative Science and Technology Initiative for Security (grant no. JPJ004596), the Iketani Science and Technology Foundation, the Kazuchika Okura Memorial Foundation, JSPS KAKENHI (grant no. 24KJ2036), and a Nihon University Research Grant for SDG-related projects (no. 24SDG02). We are grateful to G. Hatakoshi and H. Haneda for their effective scientific discussions on our manuscript and Y. Tomitsuka for supporting PL measurements.

Notes and references

1 A. Kojima, K. Teshima, Y. Shirai and T. Miyasaka, *J. Am. Chem. Soc.*, 2009, **131**, 6050–6051.
2 M. M. Lee, J. Teuscher, T. Miyasaka, T. N. Murakami and H. J. Snaith, *Science*, 2012, **338**, 643–647.
3 M. Saliba, T. Matsui, J.-Y. Seo, K. Domanski, J.-P. Correa-Baena, M. K. Nazeeruddin, S. M. Zakeeruddin, W. Tress, A. Abate, A. Hagfeldt and M. Grätzel, *Energy Environ. Sci.*, 2016, **9**, 1989–1997.
4 N. J. Jeon, J. H. Noh, W. S. Yang, Y. C. Kim, S. Ryu, J. Seo and S. Il Seok, *Nature*, 2015, **517**, 476–480.
5 D. Bi, W. Tress, M. I. Dar, P. Gao, J. Luo, C. Renevier, K. Schenk, A. Abate, F. Giordano, J.-P. Correa Baena, J.-D. Decoppet, S. M. Zakeeruddin, M. K. Nazeeruddin, M. Grätzel and A. Hagfeldt, *Sci. Adv.*, 2016, **2**, e150117.
6 N. Nishimura, H. Kanda, R. Katoh, A. Kogo and T. N. Murakami, *J. Mater. Chem. A*, 2024, **12**, 15631–15640.
7 N. Pant, A. Kulkarni, M. Yanagida, Y. Shirai, S. Yashiro, M. Sumiya, T. Miyasaka and K. Miyano, *ACS Appl. Energy Mater.*, 2021, **4**, 4530–4540.
8 H. Chen, F. Ye, W. Tang, J. He, M. Yin, Y. Wang, F. Xie, E. Bi, X. Yang, M. Grätzel and L. Han, *Nature*, 2017, **550**, 92–95.
9 Y. Zhou, M. Yang, W. Wu, A. L. Vasiliev, K. Zhu and N. P. Padture, *J. Mater. Chem. A*, 2015, **3**, 8178–8184.
10 X. Zheng, B. Chen, C. Wu and S. Priya, *Nano Energy*, 2015, **17**, 269–278.
11 B.-E. Cohen, S. Aharon, A. Dymshits and L. Etgar, *J. Phys. Chem. C*, 2016, **120**, 142–147.
12 B. Dong, M. Wei, Y. Li, Y. Yang, W. Ma, Y. Zhang, Y. Ran, M. Cui, Z. Su, Q. Fan, Z. Bi, T. Edvinsson, Z. Ding, H. Ju, S. You, S. M. Zakeeruddin, X. Li, A. Hagfeldt, M. Grätzel and Y. Liu, *Nat. Energy*, 2025, **10**, 342–353.
13 N. A. N. Ouedraogo, Y. Chen, Y. Y. Xiao, Q. Meng, C. B. Han, H. Yan and Y. Zhang, *Nano Energy*, 2020, **67**, 104249.
14 P. Du, J. Li, L. Wang, L. Sun, X. Wang, X. Xu, L. Yang, J. Pang, W. Liang, J. Luo, Y. Ma and J. Tang, *Nat. Commun.*, 2021, **12**, 4751.
15 Z. Shi, L. Lei, Y. Li, F. Zhang, Z. Ma, X. Li, D. Wu, T. Xu, Y. Tian, B. Zhang, Z. Yao and G. Du, *ACS Appl. Mater. Interfaces*, 2018, **10**, 32289–32297.
16 Q. Zhang, Q. Shang, R. Su, T. T. H. Do and Q. Xiong, *Nano Lett.*, 2021, **21**, 1903–1914.
17 S. F. Chichibu, K. Shima, A. Uedono, S. Ishibashi, H. Iguchi, T. Narita, K. Kataoka, R. Tanaka, S. Takashima, K. Ueno, M. Edo, H. Watanabe, A. Tanaka, Y. Honda, J. Suda, H. Amano, T. Kachi, T. Nabatame, Y. Irokawa and Y. Koide, *J. Appl. Phys.*, 2024, **135**, 185701.
18 N. Osawa, R. Takahashi and M. Lippmaa, *Appl. Phys. Lett.*, 2017, **110**, 263902.
19 S. Kawasaki, R. Takahashi and M. Lippmaa, *J. Phys. Chem. C*, 2019, **123**, 15551–15556.
20 S. Kawasaki, R. Takahashi, T. Yamamoto, M. Kobayashi, H. Kumigashira, J. Yoshinobu, F. Komori, A. Kudo and M. Lippmaa, *Nat. Commun.*, 2016, **7**, 11818.
21 Y. Takeyama, S. Mantoku, S. Maruyama and Y. Matsumoto, *CrystEngComm*, 2014, **16**, 684–689.
22 S. Maruyama, Y. Takeyama, H. Taniguchi, H. Fukumoto, M. Itoh, H. Kumigashira, M. Oshima, T. Yamamoto and Y. Matsumoto, *ACS Nano*, 2010, **4**, 5946–5952.
23 S. Yaginuma, K. Itaka, M. Haemori, M. Katayama, K. Ueno, T. Ohnishi, M. Lippmaa, Y. Matsumoto and H. Koinuma, *Appl. Phys. Express*, 2008, **1**, 015005.
24 K. Kawashima, Y. Okamoto, O. Annayev, N. Toyokura, R. Takahashi, M. Lippmaa, K. Itaka, Y. Suzuki, N. Matsuki and H. Koinuma, *Sci. Technol. Adv. Mater.*, 2017, **18**, 307–315.
25 T. Miyadera, T. Sugita, H. Tampo, K. Matsubara and M. Chikamatsu, *ACS Appl. Mater. Interfaces*, 2016, **8**, 26013–26018.
26 T. Dazai, T. Sato, H. Koinuma, R. Katoh and R. Takahashi, *ACS Appl. Electron. Mater.*, 2023, **5**, 3965–3972.
27 R. Takahashi, T. Kuroda, T. Dazai, T. Sato and H. Koinuma, *J. Appl. Phys.*, 2022, **131**, 175302.
28 Y. Matsubara, K. S. Takahashi, Y. Tokura and M. Kawasaki, *Appl. Phys. Express*, 2014, **7**, 125502.
29 B. Jalan, P. Moetakef and S. Stemmer, *Appl. Phys. Lett.*, 2009, **95**, 032906.
30 R. Takahashi and M. Lippmaa, *ACS Appl. Mater. Interfaces*, 2017, **9**, 21314–21321.
31 I. Ohkubo, Z. Hou, J. N. Lee, T. Aizawa, M. Lippmaa, T. Chikyow, K. Tsuda and T. Mori, *Mater. Today Phys.*, 2021, **16**, 100296.
32 R. Shimizu, S. Kobayashi, Y. Watanabe, Y. Ando and T. Hitosugi, *APL Mater.*, 2020, **8**, 111110.
33 Y. K. Wakabayashi, T. Otsuka, Y. Krockenberger, H. Sawada, Y. Taniyasu and H. Yamamoto, *APL Mater.*, 2019, **7**, 101114.
34 A. G. Kusne, H. Yu, C. Wu, H. Zhang, J. Hattrick-Simpers, B. DeCost, S. Sarker, C. Oses, C. Toher, S. Curtarolo, A. V. Davydov, R. Agarwal, L. A. Bendersky, M. Li, A. Mehta and I. Takeuchi, *Nat. Commun.*, 2020, **11**, 5966.
35 M. Lu, H. Ji, Y. Zhao, Y. Chen, J. Tao, Y. Ou, Y. Wang, Y. Huang, J. Wang and G. Hao, *ACS Appl. Mater. Interfaces*, 2023, **15**, 1871–1878.
36 Y. Chen, P. Long, B. Liu, Y. Wang, J. Wang, T. Ma, H. Wei, Y. Kang and H. Ji, *J. Mater. Chem. A*, 2024, **12**, 30249–30268.

37 M. Lu, H. Ji, Y. Chen, F. Gao, B. Liu, P. Long, C. Deng, Y. Wang and J. Tao, *J. Mater. Chem. C*, 2024, **12**, 8893–8900.

38 S. Suzuki, T. Dazai, Y. Yamamoto, H. Koinuma and R. Takahashi, *Jpn. J. Appl. Phys.*, 2023, **62**, 117001.

39 R. Takahashi, K. Valset, E. Folven, E. Eberg, J. K. Grepstad and T. Tybell, *Appl. Phys. Lett.*, 2010, **97**, 081906.

40 T. Masuda, T. Sato, M. Lippmaa, T. Dazai, N. Sekine, I. Hosako, H. Koinuma and R. Takahashi, *J. Appl. Phys.*, 2024, **135**, 095303.

41 M. Kawasaki, K. Takahashi, T. Maeda, R. Tsuchiya, M. Shinohara, O. Ishiyama, T. Yonezawa, M. Yoshimoto and H. Koinuma, *Science*, 1994, **266**, 1540–1542.

42 S. Kawasaki, E. Holmström, R. Takahashi, P. Spijker, A. S. Foster, H. Onishi and M. Lippmaa, *J. Phys. Chem. C*, 2017, **121**, 2268–2275.

43 S. Ohashi, M. Lippmaa, N. Nakagawa, H. Nagasawa, H. Koinuma and M. Kawasaki, *Rev. Sci. Instrum.*, 1999, **70**, 178–183.

44 Y. Tomitsuka, T. Saito and R. Katoh, *J. Phys. Chem. C*, 2025, **129**, 9413–9419.

45 R. Konno, S. Maruyama, T. Kosaka, R. Katoh, R. Takahashi, H. Kumigashira, N. Ichikuni, H. Onishi and Y. Matsumoto, *Chem. Mater.*, 2021, **33**, 226–233.

46 S. Nakajima and R. Katoh, *J. Mater. Chem. A*, 2015, **3**, 15466–15472.

47 R. Kumagai, R. Koguchi, T. Dazai, T. Sato, H. Koinuma, R. Katoh and R. Takahashi, *Sci. Technol. Adv. Mater.*, 2025, **26**, 2554045.

48 S. Liu, Y. Chen, W. Gao, W. Li, X. Yang, Z. Li, Z. Xiao, Y. Liu and Y. Wang, *Adv. Mater.*, 2023, **35**, 2303544.

49 B. Yuan, H. Wei, J. Li, Y. Zhou, F. Xu, J. Li and B. Cao, *ACS Appl. Electron. Mater.*, 2021, **3**, 5592–5600.

50 J. Chen, D. J. Morrow, Y. Fu, W. Zheng, Y. Zhao, L. Dang, M. J. Stolt, D. D. Kohler, X. Wang, K. J. Czech, M. P. Hautzinger, S. Shen, L. Guo, A. Pan, J. C. Wright and S. Jin, *J. Am. Chem. Soc.*, 2017, **139**, 13525–13532.

51 R. R. Lunt, J. B. Benziger and S. R. Forrest, *Adv. Mater.*, 2010, **22**, 1233–1236.

52 F. Vietmeyer, P. A. Frantsuzov, B. Janko and M. Kuno, *Phys. Rev. B: Condens. Matter Mater. Phys.*, 2011, **83**, 115319.

53 R. Katoh and K. Seki, *J. Chem. Phys.*, 2024, **160**, 174704.

54 T. J. Savenije, D. Guo, V. M. Caselli and E. M. Hutter, *Adv. Energy Mater.*, 2020, **10**, 1903788.

55 Y. Bi, E. M. Hutter, Y. Fang, Q. Dong, J. Huang and T. J. Savenije, *J. Phys. Chem. Lett.*, 2016, **7**, 923–928.

56 E. M. Hutter, R. J. Sutton, S. Chandrashekar, M. Abdi-Jalebi, S. D. Stranks, H. J. Snaith and T. J. Savenije, *ACS Energy Lett.*, 2017, **2**, 1901–1908.

57 H. Hempel, T. J. Savenjie, M. Stolterfoht, J. Neu, M. Failla, V. C. Paingad, P. Kužel, E. J. Heilweil, J. A. Spies, M. Schleuning, J. Zhao, D. Friedrich, K. Schwarzburg, L. D. A. Siebbeles, P. Dörflinger, V. Dyakonov, R. Katoh, M. J. Hong, J. G. Labram, M. Monti, E. Butler-Caddle, J. Lloyd-Hughes, M. M. Taheri, J. B. Baxter, T. J. Magnanelli, S. Luo, J. M. Cardon, S. Ardo and T. Unold, *Adv. Energy Mater.*, 2022, **12**, 2102776.

58 M. C. Gélvez-Rueda, M. B. Fridriksson, R. K. Dubey, W. F. Jager, W. van der Stam and F. C. Grozema, *Nat. Commun.*, 2020, **11**, 1901.

59 K. Cho, Y. Park, H. Jo, S. Seo, J. Moon, S. J. Lee, S. Y. Park, S. J. Yoon and J. Park, *J. Phys. Chem. Lett.*, 2024, **15**, 5795–5803.

60 L. A. Muscarella, E. M. Hutter, S. Sanchez, C. D. Dieleman, T. J. Savenije, A. Hagfeldt, M. Saliba and B. Ehrler, *J. Phys. Chem. Lett.*, 2019, **10**, 6010–6018.

61 S. Suzuki, T. Dazai, T. Tokunaga, T. Yamamoto, R. Katoh, M. Lippmaa and R. Takahashi, *J. Appl. Phys.*, 2024, **135**, 195302.

62 R. Takahashi, T. Yamamoto and M. Lippmaa, *Cryst. Growth Des.*, 2021, **21**, 5017–5026.

63 R. Katoh, A. Huijser, K. Hara, T. J. Savenije and L. D. A. Siebbeles, *J. Phys. Chem. C*, 2007, **111**, 10741–10746.

64 A. Bojtor, D. Krisztián, F. Korsós, S. Kollarics, G. Paráda, T. Pinel, M. Kollár, E. Horváth, X. Mettan, H. Shiozawa, B. G. Márkus, L. Forró and F. Simon, *Adv. Energy Sustainability Res.*, 2024, **5**, 2400043.

65 K. T. Munson, C. Grieco, E. R. Kennehan, R. J. Stewart and J. B. Asbury, *ACS Energy Lett.*, 2017, **2**, 651–658.